

## Research Article

## Open Access

Konstantinos Topouzelis\*, Suman Singha, and Dimitra Kitsiou

# Incidence angle Normalization of Wide Swath SAR Data for Oceanographic Applications

DOI 10.1515/geo-2016-0029

Received Oct 05. 2015; accepted Feb 20, 2016

**Abstract:** A backscattering trend in the range direction of the signal received by Synthetic Aperture Radar (SAR) in Wide Swath (WS) mode results in a progressive reduction of brightness over images from near to far range, which affects the detection and classification of sea surface features on wide swath SAR images. The aim of the present paper is to investigate methods for limiting the issue of Normalized Radar Cross-Section (NRCS or  $\sigma_0$ ) variation due to the incidence angle. Two sensor independent functions are investigated: a theoretical backscattering shape function derived from a minimum wind speed and an empirical range fit of NRCS against incidence angle  $\theta$ . The former method exploits only the modeled NRCS values while the latter only the image content. The results were compared with the squared cosine correction, the most widely applied method for normalization, using six newly developed comparison factors. The results showed that the cosine squared normalization has the lowest efficiency while the proposed methods have similar behaviors and comparable results. Nevertheless, after the log-transformation and summation of the comparison factors, it was clearly shown that theoretical normalization performance is superior to the empirical one since it has the highest accuracy and requires less computational time.

**Keywords:** Ocean; Oceanic Phenomena Recognition; ASAR; Normalized Radar Cross Section

## 1 Introduction

SAR imagery has proved very effective for observing, measuring and quantifying oceanographic phenomena such as fronts, waves, eddies, winds, storms, oil spills, algae blooms, currents, and boundary layer rolls [1, 2]. The ability of SAR sensors in retrieving data in almost all weather conditions, independently of sunlight surface, is extremely important for oceanographic studies.

The quality of SAR imagery is dependent on the mode of acquisition and raw data processing [3]. Oceanographic phenomena were tracked by spaceborne SAR systems, which cover wide areas, therefore the ScanSAR acquisition mode is mainly used. In the bibliography, the spatial scale of several oceanic processes which mostly lies within tens to hundreds of kilometers has already been described [4]. An example of ScanSAR mode is ENVISAT's Wide Swath Mode (WSM) with 150 m resolution, a swath width of 405 km and two possible mutually exclusive polarizations (VV or HH). The main issue related to wide swath SAR images is the progressive decrease of backscatter energy from near to far range (Figure 1). The Normalized Radar Cross-Section (NRCS) values derived from SAR images depend on the content of the observed scene as well as the sea and atmospheric conditions at the time of observation [5–7]. Also, NRCS depends on the relative azimuth angle between the radar look direction and wind direction. This means that NRCS at low incidence angles over a certain wind speed and direction is different from that at high incidence angles. Therefore, a normalization is required in order to limit the NRCS variation over the various incidence angles, since:

- Operators need to visualize the image in a more usable way in order to identify ocean phenomena through visual interpretation. It should be mentioned that the operational service for oil spill detection “CleanSeaNet”, from the European Maritime Safety Agency (EMSA), is primarily based on visual inspection [8].
- Normalization can be considered as a pre-processing step for semi or fully automatic classification systems. For example, the first crucial step

\*Corresponding Author: Konstantinos Topouzelis: Department of Marine Sciences, School of the Environment, University of the Aegean, University Hill, 81100, Mytilini, Lesvos Island, Greece; Email: topouzelis@marine.aegean.gr; Tel.: +30 22510 36878; Fax: +30 22510 36809

Suman Singha: Remote Sensing Technology Institute, German Aerospace Center (DLR), Heinrich Focke Str. 4, 28199 Bremen, Germany; Email: Suman.Singha@dlr.de

Dimitra Kitsiou: Department of Marine Sciences, School of the Environment, University of the Aegean, University Hill, 81100, Mytilini, Lesvos Island, Greece; Email: dkit@aegean.gr

for mesoscale oceanographic phenomena detection and classification (*e.g.* oil spills, eddies, currents, or fronts) is the identification of dark objects in SAR images [4, 9, 10]. This step is extremely difficult in wide swath images due to backscatter decrease from near to far range. In addition, normalization can be used for inter-comparison of many SAR images or data from the same or different sensor; the transition from one type of data to another will be simpler and more efficient after normalization, as the appearance of dark features will be similar.

The most widely used incidence angle correction technique is the square cosine correction [11]. The model is based on Lambert's law for optics and includes two assumptions; the amount of power that is radiated back to the satellite sensor follows a cosine law and the radiation variability as a function of the observed area is also cosine dependent [12]. The backscatter normalized radar cross-section in angle  $\theta$  ( $\sigma_\theta^0$ ) is related to the cosine squared of the incidence angle:

$$\sigma_\theta^0 = \sigma_0^0 \cos^2(\theta) \quad (1)$$

where  $\sigma_0^0$  is the backscatter independent of the incidence angle. Assuming a reference angle  $\theta_{ref}$  to which the image will be normalized, equation (1) is applied. Then, after dividing by parts, the radar response to  $\sigma_{ref}^0$  is given by:

$$\sigma_{ref}^0 = \frac{\sigma_\theta^0 \cos^2(\theta_{ref})}{\cos^2(\theta)} \quad (2)$$

Recent studies updated the square power of equation (2) over particular types of observation. For example in [13] a power index between 1 and 2 was applied characterizing the surface roughness over tropical forest areas. In [12] values varied between 0.2 and 3.4 depending on vegetation type and season, for savanna-dominated areas. In [14] values 10+ over water were applied for the relationship of local incidence angle with  $\sigma^0$  values. However, the square cosine correction is valid for surfaces with Lambertian reflectance properties and is not expected to perform in a satisfactory way over the sea. Another method of normalization can be based on backscatter modeling. Backscatter energy over the sea surface is strongly related to the incidence angle and wind speed and presents a broad range of backscatter levels:  $-40 \text{ dB} < \sigma^0 < +10 \text{ dB}$  from far to near range. Ocean backscatter modeling is often described by the Bragg model [15–18], which is appropriate for intermediate incidence angles (approximately  $20^\circ$ – $60^\circ$ ) and describes scattering from short gravity–capillary waves at the C-band wavelength. This model is based on physical principles rather than on an empirical relationship and calculates the  $\sigma^0$  values based on geometric and

hydrodynamic modulation. The Bragg scattering model is widely applied, however, neither the measured  $\sigma^0$  values for specific combinations of radar parameters and environmental conditions nor their observed variation can be explained satisfactorily by pure Bragg scattering theory [18]. A more advanced microwave backscatter model is described by [17]. The main advantage of that model is the breaking down of the sea surface into small, intermediate and large scale waves. Scattering from small scale waves is explained by Bragg scattering, from large-scale waves by quasi-specular scattering and from intermediate waves by Kirchhoff scattering [17]. The transition from Bragg to Kirchhoff scattering is dependent on the incidence angle, wind speed and the surface wave spectrum [17, 19]. These models refer to scattering from “pure” roughness. However, ocean roughness described by gravity–capillary and short gravity waves is always influenced by surface, subsurface and atmospheric layer processes. Therefore, the real  $\sigma^0$  value derived over a particular sea area cannot be efficiently described by stochastic modeling.

In a recent previous study [1], a theoretical backscattering shape function was introduced for normalizing WSM SAR images over the ocean. In the present work, a quantitative study is presented where the robustness of the proposed method is examined. The aim of this paper is to reveal a simple but consistent scheme for reducing the dynamic range of SAR images by removing the mean incidence angle dependence. The proposed normalization approach aims to normalize the wide swath SAR image to a fixed reference angle. The approach needs to be robust, accurate, easily applicable and transferable for different SAR oceanographic applications. A detailed description of the proposed methods is provided in the next section, followed by data sets and the comparison factors (section 4). In Section 5 the results of the proposed methodologies and further analysis are presented. The discussion of the results and conclusions are given in Section 6.

## 2 Methodology

The SAR image profile in the range direction shows a squared cosine shape function with respect to the incidence angle  $\theta(\cos^2 \theta)$  under the same wind conditions. After calibration and quantification in logarithmic scale (dB), the backscattering profile is transformed into a linear shape (Figure 1). This linearity can be questioned whenever a non-stable sea state is present. However, all examined case studies support the linear transformation. For example in Figure 1b the regression analysis revealed a

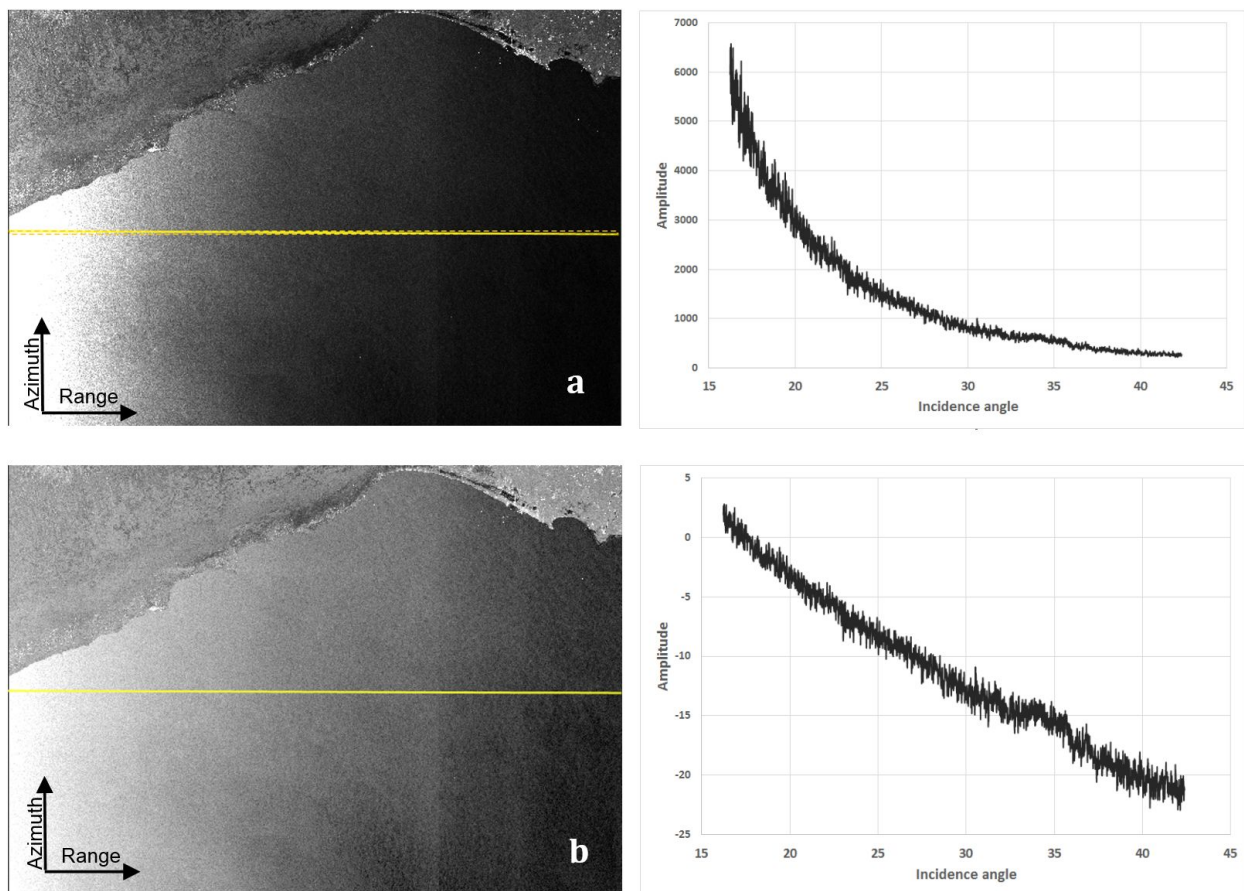


**Figure 1:** An example of ENVISAT ASAR Wide Swath Mode over sea area (Egyptian Coast, acquisition date: 13/03/11) with relatively stable wind speed of 6.5 m/s over 400 km in the range direction. Wind measured directly from the image using the CMOD-5 geophysical model. (a) Amplitude image and its profile and (b) Calibrated image and its profile.

correlation coefficient ( $R^2$ ) of 0.9801 for linear fit, 0.986 for logarithmic fit and 0.9866 for a quadratic polynomial. Since the  $R^2$  difference between the different fit lines is on the third decimal number and our scope is to produce a simple and robust normalization method, the linear shape of the backscattering profile was adapted. This linear shape in the range direction is unique for each ASAR image since it is related to the current wind speed and oceanographic phenomena. The proposed normalization approaches use the idea of inverse functions to reverse the extracted profile in slant range. The inverse function of the profile is a hypothetical function describing the increase of backscattering values in the range profile in the symmetrically opposite way to the real decrease. If the inverse function is known, then it can be directly applied for flattening the illumination in slant range. Therefore, the problem is to derive the inverse function with a specific incidence angle for the given SAR images.

The inverse function can be derived using an additive inversion. An additive inversion adds the inverse function

to create an identity function (i.e., a function that always returns the same value). Additive normalization averages the basic and the symmetric functions according to:

$$\sigma_{\theta_{ref}}^0 = \frac{\sigma_\theta^0 + (\sigma_\theta^0)^{-1}}{2} \quad (3)$$

where  $\sigma_{\theta_{ref}}^0$  is the normalized radar cross-section at an incidence angle of reference,  $\theta_{ref}$ ,  $\sigma_\theta^0$  is a specific linear function describing the relation of  $\sigma^0$  values and incidence angle ( $\theta$ ) and  $(\sigma_\theta^0)^{-1}$  is the symmetric function of  $\sigma_\theta^0$ . The linear function  $(\sigma_\theta^0)$  describing the relation of  $\sigma^0$  values and incidence angle ( $\theta$ ) for a SAR image over the sea is given by:

$$\sigma_\theta^0 = a\theta + b \quad (4)$$

with  $a$  and  $b$  being the linear coefficients. The symmetric function  $(\sigma_\theta^0)^{-1}$  of equation (4) to angle of reference ( $\theta_{ref}$ ) is:

$$(\sigma_\theta^0)^{-1} = -a\theta + 2a\theta_{ref} + b \quad (5)$$

Symmetric functions can be calculated for any incidence angle, but usually the mean angle of incident is used. The radiometric normalization function should always be preserved so that the actual  $\sigma_\theta^0$  values can be derived. This is crucial, for example, in wind field retrieval and other oceanographic applications. In the present paper, two correction approaches against the well-known cosine squared were examined: a theoretical backscattering shape function derivation based on instrument incidence angle properties and an empirical range fit of  $\sigma^0$  based on image content properties.

## 2.1 Theoretical backscattering shape function derivation

It is well known that  $\sigma^0$  values depend on the sea roughness and therefore the sea state [17]. A simple assumption regarding the scattering mechanism is necessary, since it is not possible to measure the dependence of the NRCS on the incidence angle for all possible sea states: the  $\sigma^0$  values will be normalized for the Bragg sea resonant wavelength. Therefore a stable sea state is assumed for the wide swath cover (e.g. 400 km) and all backscatter variations are altered from that sea state. For example, according to Bragg scattering theory, the resonant sea wavelengths ( $\lambda$ ) for ENVISAT ASAR WSM images captured in the C-band of the 5.6 cm wavelength and at incidence angles of approximately  $15^\circ$ – $45^\circ$  are in the range of 10.8–3.4 cm [18]. Hereafter, a second assumption that the incidence angle of  $\theta_{ref} = 30^\circ$  is the most appropriate angle for image normalization is necessary. This presents a symmetry in the angle between near and far range geometry. Therefore, the Bragg resonant sea wavelength of 5.6 cm is assumed as the primary scattering wavelength for all incidence angles. The normalization of  $\sigma^0$  at  $\theta_{ref} = 30^\circ$  will result in a new image of  $\sigma_{\theta_{ref}}^0$  values that are all hypothetically acquired at  $30^\circ$  and represent the sea wavelength of 5.6 cm. The latter is of significant importance when a physical examination of normalized SAR data is carried out for several oceanographic phenomena like oil spills, currents, wind shadow areas, upwelling zones, etc.

Considering the theoretical values of  $\sigma^0$  for the sea surface, scattering from the surface at the C-band at several incidence angles should be calculated for normalizing at  $30^\circ$ . This procedure requires modeling and measurements of the normalized radar cross-section of the sea surface at several wind speeds [19–22] and wind directions [23]. The NRCS values can be correlated with wind speeds and are dependent on polarization, upwind or downwind direction and incidence angle [20]. This correlation is multi-

variable and remains an open question among the scientific community. However, it is well known that the minimum sea wind speed for generating Bragg resonant sea waves of  $\lambda = 5.6$  cm is 1.5–2 m/s [22]. At this point, a third assumption is made regarding the existing wind speed: the incidence angle correction is based on a wind speed of 3 m/s. This assumption is necessary for correlating theoretical  $\sigma^0$  for the several incidence angles. This particular wind speed is chosen for three reasons: a) The Bragg waves are essential for having a backscatter signal. Lower wind speeds would indicate an almost flattened sea surface or one with very small capillary waves not capable of generating waves with the necessary wavelengths, b) It presents an almost perfect linear relationship between  $\sigma^0$  [dB] and  $\theta$  for incidence angles from  $15^\circ$ – $45^\circ$  as opposed to higher wind speeds. This assumption makes calculations simpler. Polynomials describing the relationship  $\sigma^0$ – $\theta$  from higher wind speeds are difficult to compare, c) A wind speed of 3 m/s is of particular importance for  $\sigma^0$  values in the far range because it provides scattering values less than –17.5 dB. On the contrary, higher wind speeds do not generate such values resulting in lowering dynamic range correction; a wind of 7 m/s (the mean global wind speed), would reduce the dynamic range correction of NRCS values of about 3.5 dB.

The  $\sigma^0$  values of 3 m/s wind speed was measured during airborne experiments and illustrated [11, 24]. The  $\sigma^0$  values follow a linear distribution for incidence angle  $\theta$  between  $16^\circ$  and  $45^\circ$ . For those two angles, the  $\sigma^0$  values are 2.5 dB and –20 dB respectively. Therefore, the theoretical  $\sigma^0$  values for  $\theta$  between  $16^\circ$  and  $45^\circ$  are given by:

$$\sigma_\theta^0 = -0.776\theta + 14.914 \quad (6)$$

The symmetric equation to the incidence angle of  $\theta = 30^\circ$  is given according to (5) by:

$$\left(\sigma_{\theta(30^\circ)}^0\right)^{-1} = 0.776\theta - 31.638 \quad (7)$$

Finally, the theoretical normalized  $\sigma_{REF(30^\circ)}^0$  for the  $\theta_{ref} = 30^\circ$  can be calculated for all datasets according to (3) using the real  $\sigma_\theta^0$  measurements of SAR images and the symmetric equation of (7).

Theoretical backscattering shape function derivation can be considered as a theoretical backscattering profile in the range direction because it only uses information from the image geometry, i.e., its incidence angle  $\theta$  and the theoretical  $\sigma^0$  value at a specified wind speed.

## 2.2 Empirical range fit

NRCS ( $\sigma^0$ ) values can be directly used to calculate the mean image profile against the incidence angle. The backscattering profile is dependent on the image content and is calculated by along-track averages, *i.e.*, averaging pixel values of each image column and excluding land area present in the image. Image profile can be seen by a scatter plot of  $\sigma^0$  values against incidence angle  $\theta$ . Since all values are included in the scatter plot, an averaging of  $\sigma^0$  values for each incidence angle is needed to calculate the image profile. A linear regression analysis is used for extracting the exact profile. Then, an inverse function is calculated according to (5) and the normalization process is applied according to (3). The present normalization function generation differs from the theoretical one since the source of the relationship between  $\sigma^0$  values and incidence angles is dependent on image content (*i.e.*, any mesoscale oceanographic phenomena). Therefore, its benefit is that no additional data are required either for the sea clutter distribution or for the theoretical-modeled backscatter values of the sea surface.

## 3 Data Set

An evaluation of the normalization techniques proposed in this paper was carried out using 30 ASAR Wide Swath Mode (WSM) images from the ENVISAT satellite at VV polarization, operating at C-band. SAR images (apart from normalization) were selected for the study of atmospheric phenomena in sea surface [1]. This was ideal for examining the proposed methods in a complex sea environment because the main challenge was to reveal phenomena not visible before normalization. The ASAR WSM dataset was generated from data collected in the ScanSAR mode. This type of product includes slant range to ground range corrections, and it covers a continuous area along the imaging swath of approximately 400 km. The pixel size of the images was  $75 \times 75$  m. The incidence angle was approximately  $15^\circ$  to  $45^\circ$  and the image cover was approximately 400 km in the slant direction and 1000 km in the azimuth direction [25]. The dataset was obtained for the year 2011.

The Aegean Sea was chosen as the case study area (Figure 2) for its unique characteristics. The Aegean Sea represents the north-eastern part of the eastern Mediterranean Sea and is characterized by a complicated hydrographical and ecological structure due to its geographical position. The study area is connected to the Sea of Marmara through the Dardanelles Straits and contains numer-

ous islands and continuously changing winds. Many types of oceanographic phenomena are observed in this study area and are represented in the acquired dataset.

Before the normalization process, calibration and a land masked operation were carried out on each SAR image. For ENVISAT ASAR WSM, the calibration algorithm is described in [26]. Land masking was performed using the Global Self-Consistent Hierarchical High-Resolution Shoreline (GSHHS) provided by NOAA [27]. Both preprocessing steps were executed within the MATLAB environment.

## 4 Comparison Factors for SAR Normalization

The comparison of the proposed methods was carried out by developing and applying six comparison factors based on the mean and variance values of specific sea areas of SAR imagery. The calculation of the comparison factors was made in  $\sigma^0$  [dB] after land masking. Comparison factors were calculated for the original images, before any normalization and after the theoretical and empirical normalizations. The first two comparison factors calculated on whole image statistic parameters. These parameters are biased by the main sea clutter contained in the area covered. For that reason the rest of the four comparison factors calculated for selected regions of interest (ROIs) parameters. Although the sea surface roughness is not constant throughout a SAR image, much effort is given to select ROIs with same sea characteristics. The comparison ROIs was chosen as objectively as possible; with the same size and wind speed, and under exactly the same pixel distance from close and far range edges. To identify the best performing normalization, the sum of the comparison factors was calculated after being log-transformed. Their values are included in the final results for highlighting the performance of the normalization methods. In the next paragraphs, these six factors are described.

### 4.1 Image coefficient of variation

After a successful normalization process, original and incidence angle corrected (*i.e.* normalized) images should present small differences in the variation of the  $\sigma^0$  values. This factor ensures that the range of information provided by the radiometrically corrected image (original) should remain as constant as possible after the incidence angle correction. The image Coefficient of Variation (CV) is de-

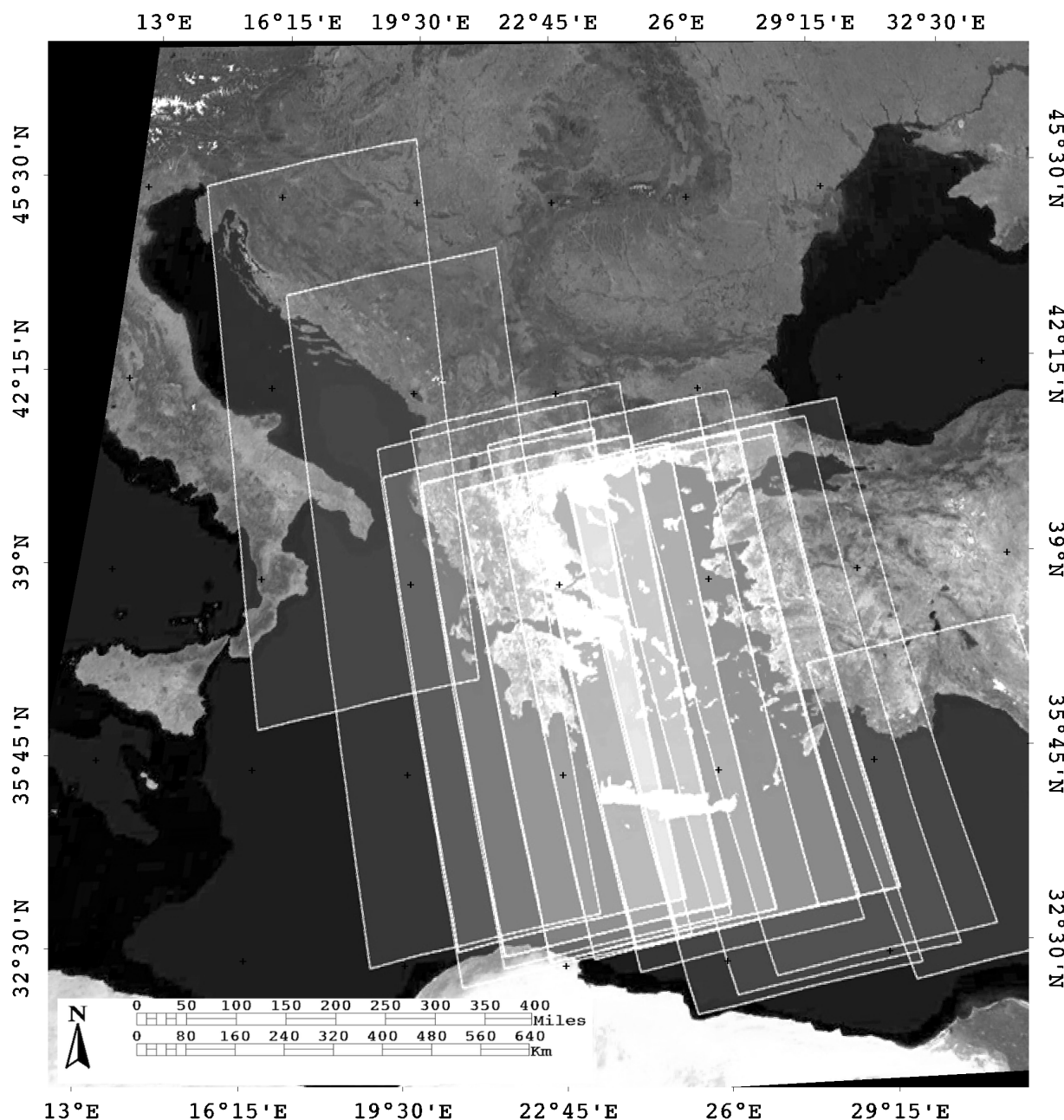


**Figure 2:** The selected area of study and dataset coverage.

fined as the ratio of the standard deviation to the mean of all  $\sigma^0$  image values. This factor is important since the normalization will alter the  $\sigma^0$  values, but their variability in relation to the mean of their population should remain relatively constant. Constant variability is important when examining the different values of roughness in the normalized image, *i.e.*, examining various oceanographic phenomena on SAR images, exactly as they would have been examined in the original image. The difference be-

tween the coefficients of variation of the original and normalized image shows the range of the change and is given by:  $CV_{diff} = CV_{original} - CV_{normalized}$  in dB.

#### 4.2 Mean column difference (along-track)

In a successful radiometric normalization,  $\sigma^0$  values should remain constant between the near and far range

over the ocean and under similar oceanographic conditions. Although it is unusual to find similar oceanographic conditions over hundreds of kilometers in SAR range direction, the mean value of  $\sigma^0$  for the first and last columns in the along-track direction of SAR images should remain close. In the near range, very high values of  $\sigma^0$  were presented due to image geometry, which cannot be taken into consideration for the comparison. Therefore, the first and the last 200 columns were omitted from the comparison, for symmetry reasons. Since a single column difference could be biased on a specific sea roughness, an average value from 100 columns was used in the near and far range. For a matrix image A represented by [i] columns, a comparison is made for average  $\sigma^0$  between columns  $A_{[200-300]}$  and  $A_{[(i-300)-(i-200)]}$ . The difference is calculated by:  $Col_{diff} = A_{[200-300]} - A_{[(i-300)-(i-200)]}$ .

### 4.3 Mean window difference

The column (along-track) difference factor may be misleading because it is dependent on the sea clutter contained in the area covered. Therefore, another comparison factor was adopted by measuring the average of  $\sigma^0$  in regions (boxes) of expected homogeneous backscattering coefficients in the near and far range. While in the mean column difference there is a high probability of containing several oceanographic phenomena (e.g., low wind vs. high wind areas), in the window difference, areas are manually selected to contain sea cluster states as similar as possible. The comparison was performed by comparing average  $\sigma^0$  in the near (NR) and far range (FR) by a user-selected area of interest. The size of the areas was  $1000 \times 1000$  pixels in NR and FR. The areas were chosen based on the criterion excluding any oceanographic phenomenon that might alter the sea roughness. A small difference implies an insufficient change in  $\sigma^0$  and therefore successful normalization and *vice versa*. The mean window (box) difference is measured by:  $Box_{diff} = Box_{FR} - Box_{NR}$  in dB.

### 4.4 Difference in radiometric error (relative)

Radiometric error ( $\delta\Gamma$ ) is a measure of the relative radiometric calibration performance. It can be estimated from the image by measuring the radiometric variation in regions of expected homogeneous backscattering coefficients. The radiometric variation is defined as the ratio of the standard deviation to the mean of the  $\sigma^0$  values of the selected area. It shows the extent of variability in relation to the mean of the  $\sigma^0$  values. A comparison of radiometric

error was performed in the near (NR) and far range (FR), for the same area of interest (box), as described above. It was measured by:  $\delta\Gamma_{diff} = \delta\Gamma_{NR} - \delta\Gamma_{FR}$  in dB. A small variation implies no substantial change in  $\sigma^0$  and therefore successful normalization. Difference in radiometric variation is calculated using selected areas only in the normalized image while the difference in coefficients of variation is calculated for whole original and normalized images.

### 4.5 Difference in signal-to-noise ratio

The signal-to-noise ratio (SNR) compares the level of a desired signal to the level of background noise. It is defined as the ratio of signal power to the noise power. It is measured as the ratio of the mean of the  $\sigma^0$  values to the standard deviation of a selected area. The difference of SNR in the near (NR) and far range (FR) was measured for the same area of interest, as described in the mean window measurement as  $SNR_{diff} = SNR_{FR} - SNR_{NR}$  in dB. The signal-to-noise ratio and radiometric error are proportional, but their difference is not. The  $SNR_{diff}$  shows the difference of mean  $\sigma^0$  taking into account the distribution of  $\sigma^0$  values, while the  $\delta\Gamma_{diff}$  shows the difference in the distribution of the  $\sigma^0$  values taking into account their starting point, *i.e.*, the mean  $\sigma^0$  value.

### 4.6 Mean transect angle

A successful normalization can be effectively measured using transects in which backscattering is relatively constant along the range direction. A first order regression analysis of the pixel transect values will produce a single line representing the general trend of the change in digital values. The angle of this line represents the degree of change and can be easily measured as constant ' $a$ ' from the  $y = ax + b$  equation of the regression line. Smaller angles represent minor changes while bigger angles represent significant changes of  $\sigma^0$  values. The mean angle of "clean" transitions, *i.e.*, transitions without the presence of any dark features, and with the same wind conditions, will yield more accurate angle calculations. Nevertheless, in most cases this is not possible because it is unlikely to find the same sea roughness (wind condition and presence of dark features) over hundreds of kilometers. For that reason, the mean transect angle of all the image lines was calculated. This value is less biased by the image content and the sea wind variation.

The aforementioned comparison factors were used to determine the success of the normalization process. All of

them have the same importance to the final results. However, each factor examines normalization from a different perspective and presents biased results compared to the rest. To evaluate the effectiveness of the different normalization processes, a more objective criterion was considered: the sum of the measured factors after log transformation. All the factors used in this study are quantitative variables with strongly varying ranges of values. Also, some measurements have heavy-tailed distributions. Based on the characteristics of the dataset, all comparison factor values were log-transformed. The ideal normalization should result in zero values for all measurements.

## 5 Results – analysis

In this section, the results produced are presented and analyzed corresponding to the six comparison factors. An example of the normalized images and their scatter plots is illustrated in Figures 3 and 4, respectively.

The difference in the coefficient of variation was found very low (maximum 0.4 dB) for all three examined methods, *i.e.*, squared cosine, additive theoretical and linear empirical fit. The latter confirms the initial claim that  $\sigma^0$  values' variability should remain relatively constant before and after normalization. However, the coefficients of variation for the three normalization methods were similar in implying that there is no significant difference among the examined methods. This result illustrates that  $\sigma^0$  values do remain relatively constant after normalization, and the actual differences of the normalization methods should be highlighted by the other comparison factors.

The absolute mean column difference (Figure 5) among the original and the normalized methods presented a relatively higher difference between the squared cosine and the other two methods. Squared cosine correction produced the worst column difference of 18 dB, while the mean column difference for the original imagery was 15 dB. This was an awkward result, since the cosine normalization produced results inferior to the original imagery. The latter can be explained by comparing the original imagery and the produced results, not only for the measured columns but for the whole image. Indeed, the cosine normalization was valid for the central part of the image but did not function correctly on the image sides (especially in the close range); therefore, cosine correction is not good enough for the edges in the range direction. On the contrary, linear and theoretical normalizations had a significant reduction (5 dB – 15 dB) in their mean column difference. Linear normalization is the one with the most sig-

nificant reduction. For all the 30 images examined, linear normalization presented a mean column difference of less than 5 dB. A similar performance was given by the theoretical normalization, with only 7 images having a column difference larger than 5 dB and in all cases smaller than 8 dB.

Concerning the difference, the variation of  $\sigma^0$  due to the existence of several oceanographic phenomena cannot be avoided. On the contrary, the next three comparison factors (*i.e.* mean window, radiometric error and signal-to-noise ratio differences) were based on image windows in the near and far range, selected by the criterion of representing the same sea condition as far as possible. The absolute differences in the mean window were quite similar to the mean column difference. The linear and theoretical corrections presented small differences, mostly lower than 5 dB. In the case of linear normalization, only four images presented a higher difference than 5 dB, with the maximum being 6.18 dB. In the case of the theoretical normalization, three images exceeded the 5 dB difference, but their values ranged from 7.5 to 8.6 dB. Noteworthy were the minimum values of theoretical normalization compared to those of linear normalization. For the former, eight out of thirty examined cases were less than 1 dB, while for the latter only four. The opposite behavior was observed for the squared cosine normalization. The differences for most of the cases were lower than the original image. The same explanation can be given for column difference. While the cosine normalization works to a relatively satisfactory level for the middle part of the image, the normalization does not perform correctly for the edges in the range direction.

The results of the radiometric error difference (Figure 6) were similar to the previous two comparison factors. The linear and theoretical normalizations had differences of less than 0.05 dB, while squared cosine normalization presented values that were mostly larger than 0.1 dB. Both the linear and theoretical normalizations performed very efficiently regarding their normalization ability. Only six images presented values larger than 0.05 dB, and these can be treated as outliers or areas with very different roughness conditions in the near and far range. In addition, squared cosine normalization did not improve the image performance at all.

The results of the signal-to-noise ratio difference had the highest differences among the comparison factors. Theoretical and linear normalization presented values less than 5 dB for the most part, while the original image and cosine correction had higher differences. The lowest differences were recorded for theoretical and linear normalization with values of almost 0.30 dB. Nevertheless, the highest differences of 18 dB were similar for all methods. The

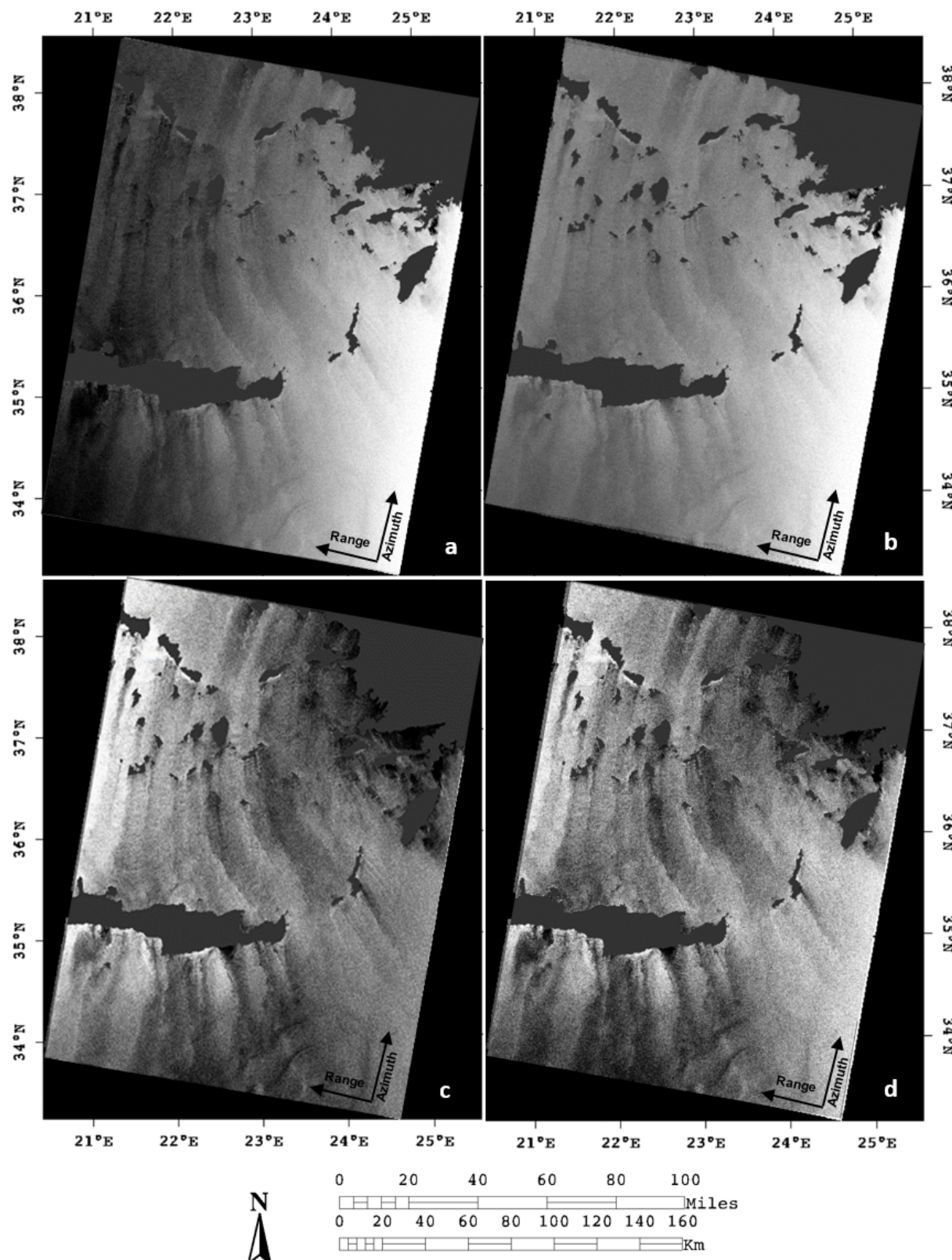


**Figure 3:** Image example of normalization: (a) L1B ASAR WSM product, (b) Squared cosine normalization, (c) Theoretical normalization, (d) Linear empirical normalization.

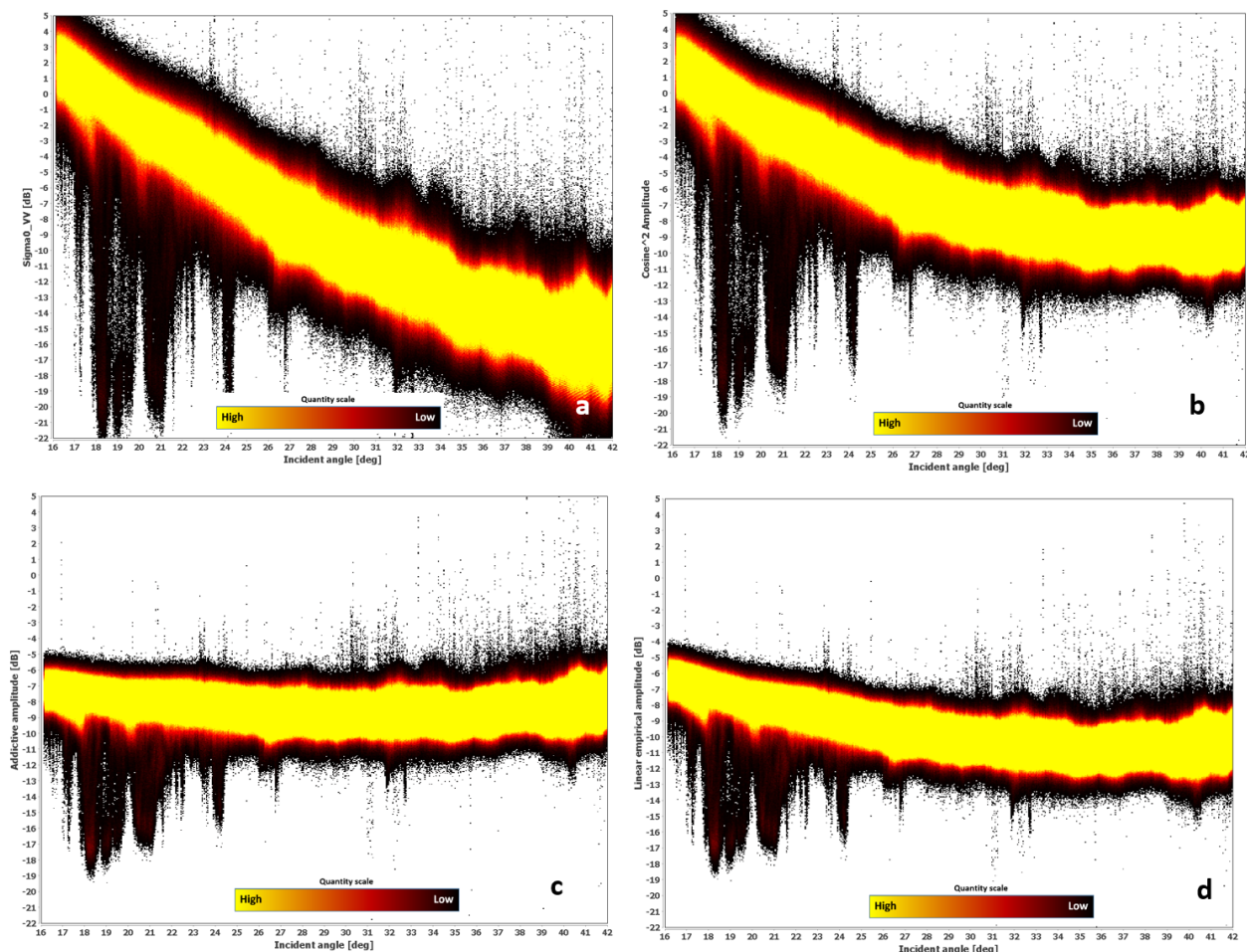


**Figure 4:** Range profile plots from Figure 3 images: (a) L1B ASAR WSM product, (b) Squared cosine normalization, (c) Theoretical normalization, (d) Linear empirical normalization.

signal-to-noise ratio mean values were found important for the comparison. The theoretical normalization with a mean signal-to-noise ratio of 4.81 dB predominated among the remaining methods. The next best result was for the linear normalization with 6.39 dB and the worst for the cosine normalization with 10.09 dB (worse than the original image of 9.25 dB).

The results for the constant describing the mean transect angle clearly showed the difference of cosine normalization from the theoretical and the linear methods. The constant of the mean angle of the cosine correction was between 0.8 and 1.1 dB, while for the other two methods it was almost stable at 0.1 dB. The calculation of the mean transect angles clearly showed the successful normalization of ASAR images for the theoretical and linear methods and their similarities in the produced results.

The six comparison factors showed significant differences. The absolute difference of the coefficient of variation had values in the range 0.1–0.6 dB, while the mean box

difference from 0.0 to 30.00 dB. Therefore, the simple sum of the produced results would lead to biased results. The quantitative factor for successful normalization was represented by the sum of the log-transformed measurement results and is shown in Figure 7. The points represent the performance for each image and the line used to highlight the trend of the normalizations although no data exist between them. The best performing normalization is the one with the minimum sum value. Squared cosine correction is clearly not adequate for normalization above the sea. Its performance was unexpected since it did not show any difference from the original image measurements. The opposite happens for the theoretical and linear empirical fit functions, which differ by 2 to 7 dB from the original image; they have similar performance in several cases. Indeed, the performance follows a similar pattern for both normalizations, although the theoretical performance is always below the linear one. Upon a closer look, the theoretical normalization functions were much better than the linear

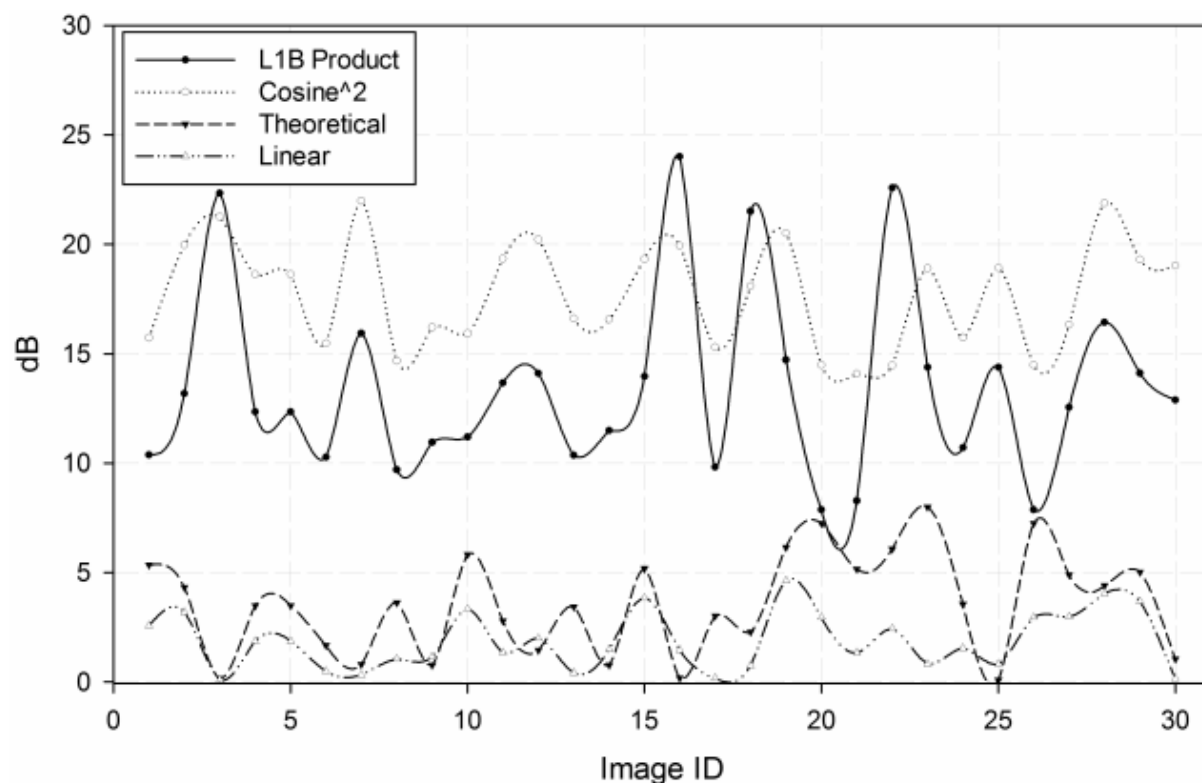


Figure 5: Results of mean column difference.

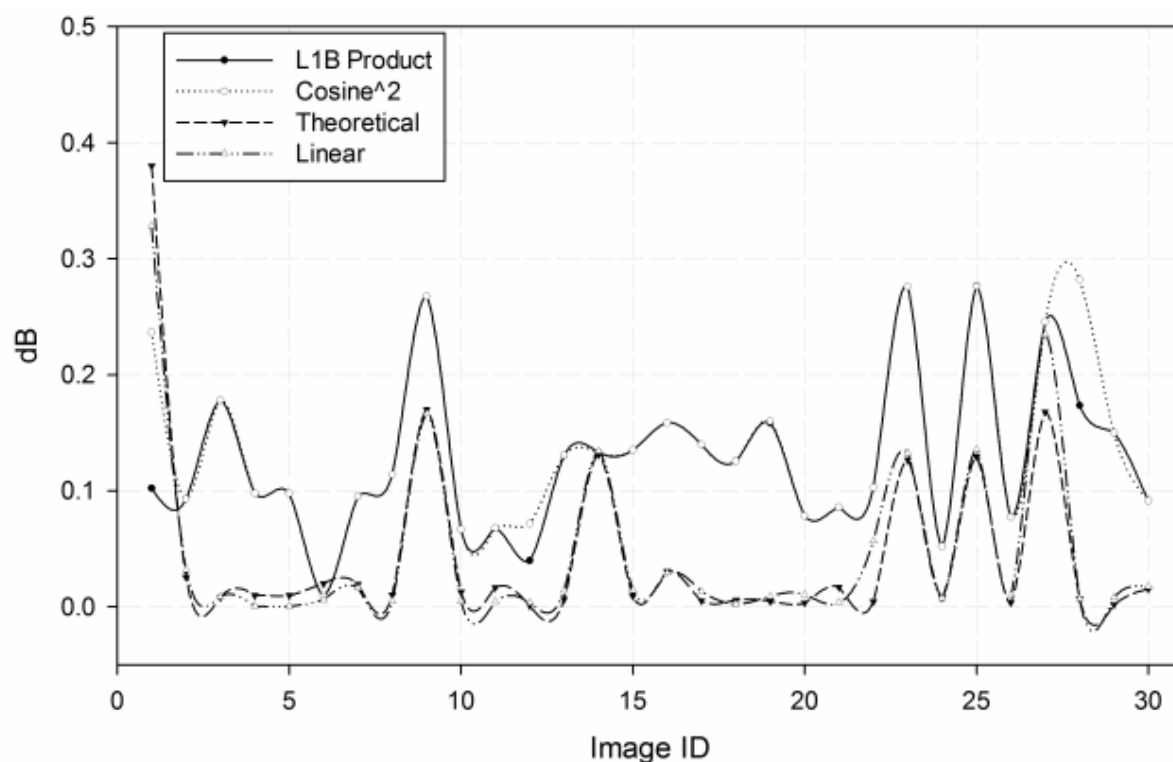
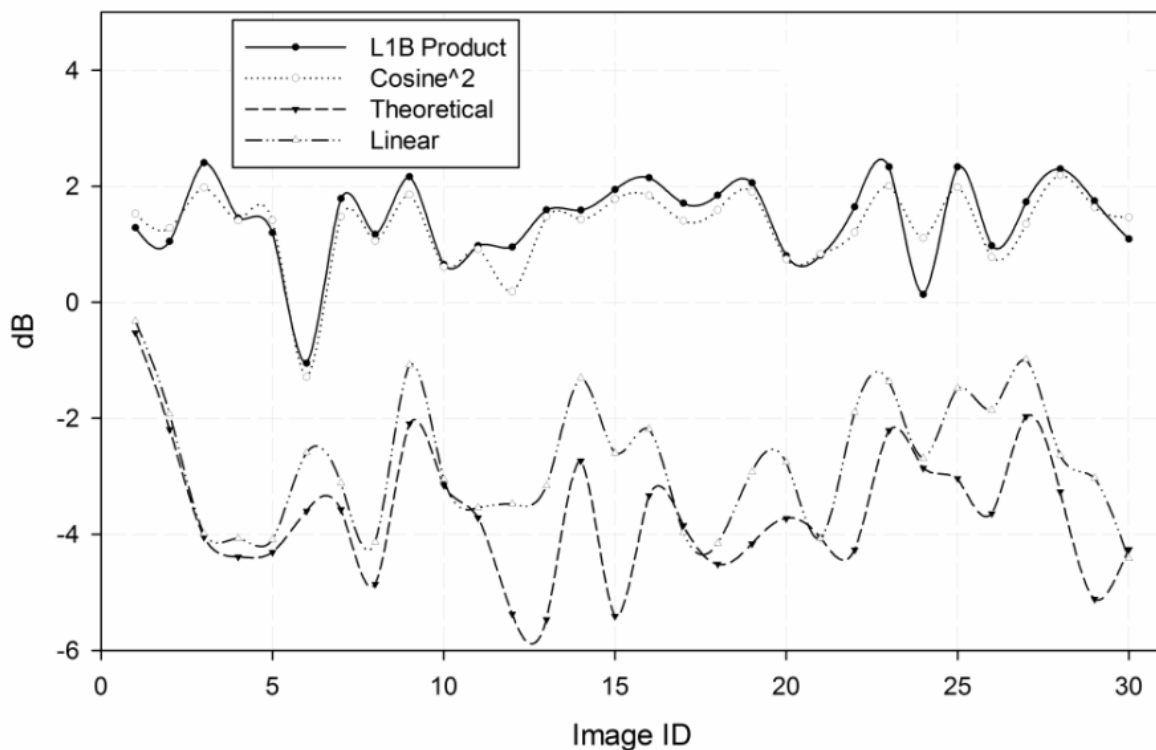


Figure 6: Results of radiometric error difference.



**Figure 7:** Results of comparison factors after summarization and log-transformation.

one. From the 30 images examined, 19 (63%) had a significant difference in performance (*i.e.*, larger than 0.5 dB) for the theoretical normalization against the linear one, and 11 images (37%) showed similar performance. Concerning those with a significant difference, the higher value was 2.8 dB and the lowest 0.55 dB, with the majority around 0.8 dB. The sum of the log transform indicated the better performance of theoretical normalization.

## 6 Conclusions – Discussion

The present paper examined different normalization functions for correcting the progressive brightness reduction of SAR WSM images in the range direction over the ocean. The problem is due to the large incidence angle variation from near to far range in WSM images which clearly affects dark spot detection for oil spill classification. Two methods were proposed for correcting the brightness reduction: the theoretical shape function derivation and the empirical range fit. Their efficiency was examined against the squared cosine correction which is based on Lambert's law for optics. The former methodology exploits a theoretical backscattering profile in the range direction formed by the

image geometry (*i.e.*, its incidence angle  $\theta$  and the theoretical  $\sigma^0$  value at a specified wind speed). It can be universally applied to all SAR sensors in ScanSAR mode since it is independent of the image content. However, its limitation is the dependence on a specific wind speed for all images. On the other hand, the empirical range fit calculates the backscattering profile by averaging the pixel values of each image column. It depends on the image content and therefore on any mesoscale oceanographic phenomena present in the image. No additional data is required either for the sea clutter distribution or for the theoretical-modeled backscatter values of the sea surface. It is image-dependent, meaning that every image has its own shape function.

The effectiveness of the normalization functions was examined in 30 wide-swath ASAR images after image calibration over the Aegean Sea. Normalization was made in the middle plane of the 30° incidence angle using six newly developed and introduced comparison factors: one refers to the image as a whole (*i.e.*, the image coefficient of variation), one to the difference in specific columns at near and far range, *i.e.*, column difference, one to the slope of image transects (*i.e.*, lines slope) and three to specific windows in the near and far range (*i.e.*, mean window differ-

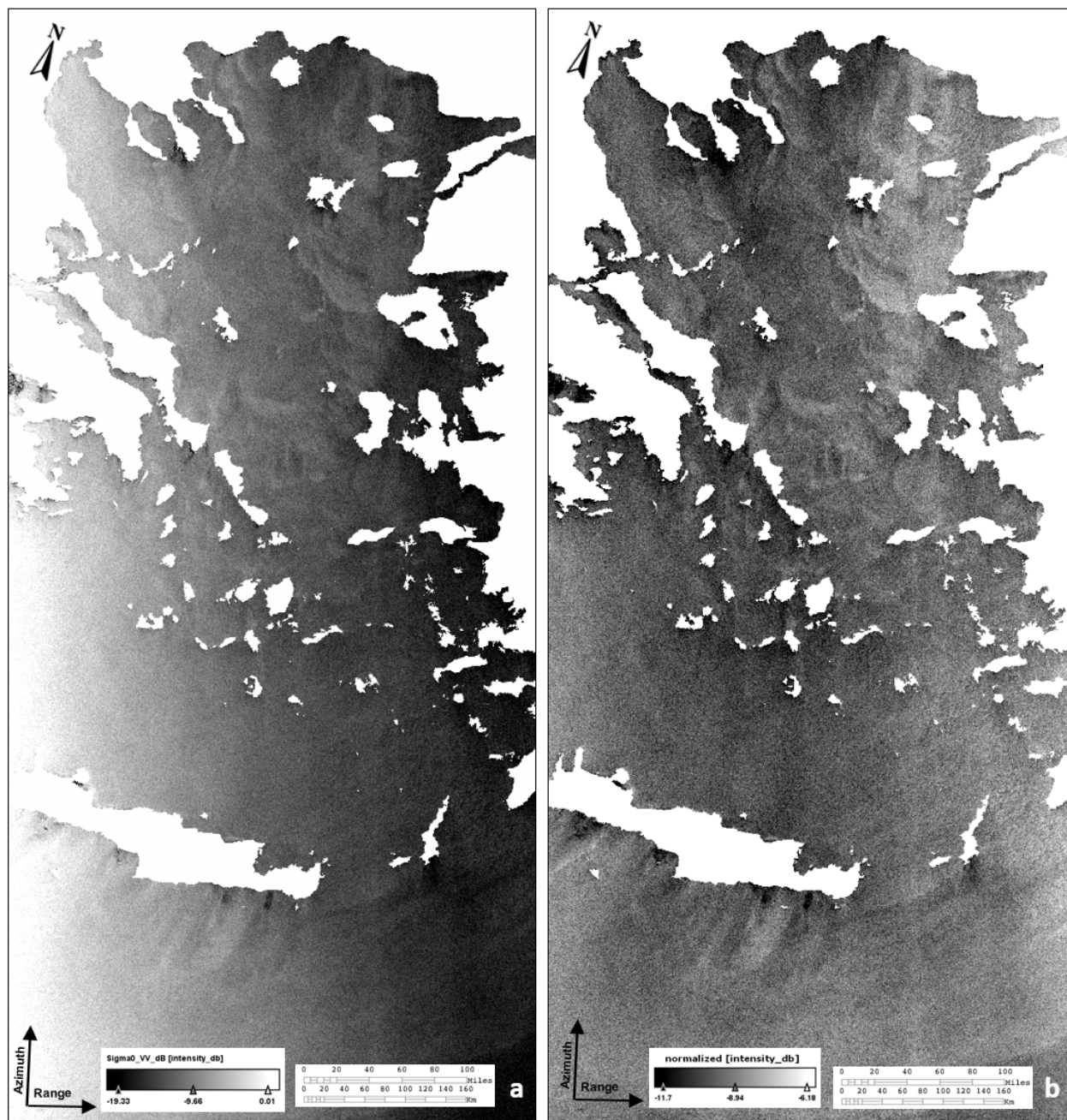


**Figure 8:** Image example of normalization: (a) L1B ASAR WSM product, (b) Theoretical normalization.

ence, radiometric error difference and signal-to-noise ratio difference).

From the present study, three main conclusions are derived. Firstly, the cosine squared normalization has the lowest efficiency and in many cases adversely affects the NRCS values in an awkward way. In general, cosine normalization works relatively well for the middle part of the ASAR image but does not perform correctly at the edges in the range direction. This can be seen from the absolute difference of the coefficient of variation, where it presents

similar results to the other two normalization methods, *i.e.*, approximately 0.1 dB. On the contrary, in the following three comparison factors cosine normalization presents worse results than the original image. Therefore, it is suggested that cosine correction cannot be used for successful normalization in wide swath SAR data.

Secondly, the theoretical and the empirical normalization functions show similar behavior and present comparable results for each comparison factor. For the image coefficient variation, both methods present high sta-

bility and a negligible difference of 0.1 dB was recorded between them. Similarly, the mean column difference highlights the high performance for both methods, with most of the images having differences of less than 5 dB between the near and far range. The mean difference between the two methods is less than 0.05 dB. Therefore, the two methods present equal effectiveness. The same behavior with negligible differences (less than 0.05 dB) was detected for the radiometric error differences and for mean transects angle measurements. Close but comparable results were presented in the mean window and signal-to-noise ratio differences. The theoretical method has better mean window difference value (2.35 dB) than the empirical one (2.45 dB). Finally, the largest difference was recorded for the radiometric error difference, where the theoretical method proved superior to the empirical one by 1.57 dB.

Therefore, taking into account the six comparison factors, it can be concluded that both the theoretical and the empirical methods perform in a reliable and robust way. Nevertheless, after the above measurements are log-transformed and summed, it is clearly shown that theoretical normalization performs better than the empirical. From the 30 SAR images used, 19 presented a better performance for the theoretical normalization than for the empirical one. The remaining 11 images showed similar performance for both normalizations. In conclusion, theoretical normalization can be chosen as the most appropriate normalization method, since it performs better, does not need any information on the image content and requires less computational time.

The outcome of the theoretical normalization function is a new image with stable NRCS values in the range direction. It can be seen as an image of the “sea roughness” directly related with the local wind stress or presence of oceanographic phenomena and can be broadly used for detecting oceanographic phenomena in Wide ScanSAR images.

However, the proposed methods present specific limitations which should be mentioned. Empirical normalization *i.e.* normalization derived from the image itself is biased by the oceanographic phenomena and might show an opposite tendency. This is intense when large phenomena are present in the images *e.g.* large low wind areas. In these cases, even image degradation is expected after normalization. On the contrary, theoretical normalization is independent of any present phenomenon. However the method and its parameters are based on limited experimental measurements which were derived in specific polarimetry and wind conditions. While the polarimetric issue can be bypassed using the same polarimetric mode, wind speed is most likely to alter in a 400 km swath. This

always happens in complicated sea environments as in the examined Aegean Sea with its numerous islands and bays. Moreover, in the experiment, the measurements which define the parameters in the theoretical normalization did not include the small differences on NRCS due to upwind or downwind sea waves direction in relation to SAR geometry acquisition.

The six comparison factors were carefully developed to represent the performance of the normalization methods, and each one examines the normalization from a different perspective. The overall performance was calculated by log transformed values of comparison factors and the summation of their values. Log transformation was chosen due to unstable scale differences in comparison factors, and summation was performed because all factors were assumed to have the same importance. The selected accuracy performance scheme was simple and effective. In a future study, a more sophisticated statistical accuracy assessment could be examined under a multi-variance logic weighting the comparison factors. In addition, in future work Wide ScanSAR images could be normalized to arbitrary values of NRCS, *e.g.*, not necessarily to the 30° reference incidence angle, and normalization could be examined for wind speeds other than 3 m/s.

The proposed methodology can be applied in new SAR sensors such as Sentinel-1 for the ScanSAR mode.

**Acknowledgement:** The authors would like to thank the European Space Agency (ESA) which provided the ENVISAT ASAR data for the study within their PI program.

## References

- [1] K. Topouzelis and D. Kitsiou, Detection and classification of mesoscale atmospheric phenomena above sea in SAR imagery, *Remote Sens. Environ.*, vol. 160, pp. 263–272, 2015.
- [2] C. Brekke and A. Solberg, Oil spill detection by satellite remote sensing, *Remote Sens. Environ.*, vol. 95, no. 1, pp. 1–13, Mar. 2005.
- [3] M. Vespe and H. Greidanus, SAR Image Quality Assessment and Indicators for Vessel and Oil Spill Detection, *IEEE Trans. Geosci. Remote Sens.*, vol. 50, no. 11, pp. 4726–4734, Nov. 2012.
- [4] D. R. Lyzenga and G. O. Marmorino, Measurement of surface currents using sequential synthetic aperture radar images of slick patterns near the edge of the Gulf Stream, *J Geophys. Res.*, vol. 103, no. C9, pp. 18769–18778, 1998.
- [5] W. Alpers and W. Huang, On the Discrimination of Radar Signatures of Atmospheric Gravity Waves and Oceanic Internal Waves on Synthetic Aperture Radar Images of the Sea Surface, *IEEE Trans. Geosci. Remote Sens.*, vol. 49, pp. 1114–1126, 2011.
- [6] X. Li, W. Zheng, C.-Z. Zou, and W. G. Pichel, A SAR Observation and Numerical Study on Ocean Surface Imprints of Atmospheric

- Vortex Streets, *Sensors*, vol. 8, no. 5, pp. 3321–3334, May 2008.
- [7] W. C. Keller, V. Wismann, and W. Alpers, Tower-based measurements of the ocean C band radar backscattering cross section, *J. Geophys. Res.*, vol. 94, no. C1, p. 924, 1989.
  - [8] EMSA, Addressing Illegal Discharges in the Marine Environment, 2013.
  - [9] S. Singha, M. Vespe, and O. Trieschmann, Automatic Synthetic Aperture Radar based oil spill detection and performance estimation via a semi-automatic operational service benchmark., *Mar. Pollut. Bull.*, vol. 73, no. 1, pp. 199–209, Aug. 2013.
  - [10] K. N. Topouzelis, Oil Spill Detection by SAR Images: Dark Formation Detection, Feature Extraction and Classification Algorithms, *Sensors*, vol. 8, no. 10, pp. 6642–6659, Oct. 2008.
  - [11] F. T. Ulaby, R. K. Moore, and A. K. Fung, *Microwave Remote Sensing: Active and Passive Volume II: Radar Remote Sensing and Surface Scattering and Emission Theory*, vol. 2, no. 2. Artech House, 1982.
  - [12] I. E. Mladenova, T. J. Jackson, R. Bindlish, and S. Hensley, Incidence Angle Normalization of Radar Backscatter Data, *IEEE Trans. Geosci. Remote Sens.*, vol. 51, no. 3, pp. 1791–1804, Mar. 2013.
  - [13] J. P. Ardila, V. Tolpekin, and W. Bijker, Angular Backscatter Variation in L-Band ALOS ScanSAR Images of Tropical Forest Areas, *IEEE Geosci. Remote Sens. Lett.*, vol. 7, no. 4, pp. 821–825, Oct. 2010.
  - [14] D. O’Grady, M. Leblanc, and D. Gillieson, Relationship of local incidence angle with satellite radar backscatter for different surface conditions, *Int. J. Appl. Earth Obs. Geoinf.*, vol. 24, pp. 42–53, Oct. 2013.
  - [15] J. Wright, A new model for sea clutter, *IEEE Trans. Antennas Propag.*, vol. 16, no. 2, pp. 217–223, Mar. 1968.
  - [16] G. R. Valenzuela, Theories for the interaction of electromagnetic and oceanic waves? A review, *Boundary-Layer Meteorol.*, vol. 13, no. 1–4, pp. 61–85, Jan. 1978.
  - [17] W. J. Plant, A stochastic, multiscale model of microwave backscatter from the ocean, *J. Geophys. Res.*, vol. 107, no. C9, p. 3120, 2002.
  - [18] R. Romeiser, W. Alpers, and V. Wismann, An improved composite surface model for the radar backscattering cross section of the ocean surface: 1. Theory of the model and optimization/validation by scatterometer data, *J. Geophys. Res.*, vol. 102, no. C11, p. 25237, 1997.
  - [19] W. J. Plant, A two-scale model of short wind-generated waves and scatterometry, *J. Geophys. Res.*, vol. 91, no. C9, p. 10735, 1986.
  - [20] V. Kudryavtsev, D. Hauser, G. Caudal, and B. Chapron, A semiempirical model of the normalized radar cross-section of the sea surface 1. Background model, *J. Geophys. Res.*, vol. 108, no. C3, p. 8054, 2003.
  - [21] M. A. Donelan and W. J. Pierson, Radar scattering and equilibrium ranges in wind-generated waves with application to scatterometry, *J. Geophys. Res.*, vol. 92, no. C5, p. 4971, 1987.
  - [22] R. Romeiser and W. Alpers, An improved composite surface model for the radar backscattering cross section of the ocean surface: 2. Model response to surface roughness variations and the radar imaging of underwater bottom topography, *J. Geophys. Res.*, vol. 102, no. C11, p. 25251, 1997.
  - [23] H. Hersbach, A. Stoffelen, and S. De Haan, CMOD5: An improved geophysical model function for ERS C-band scatterometry, *ECMWF*, no. January, pp. 1–52, 2003.
  - [24] F. Feindt, V. Wismann, W. Alpers, and W. C. Keller, Airborne measurements of the ocean radar cross section at 5.3 GHz as a function of wind speed, *Radio Sci.*, vol. 21, no. 5, pp. 845–856, Sep. 1986.
  - [25] Y.-L. Desnos, H. Laur, J. Closa, and P. Meisl, The Envisat ASAR Processor and Data Products, *SAR Work. CEOS Comm. Earth Obs. Satell. Work. Gr. Calibration Valid.*, vol. 450, 2000.
  - [26] B. Rosich and P. Meadows, Absolute Calibration of ASAR Level 1 Products Generated with PF-ASAR, *ESA/ESRIN, ENVI-CLVL-EOPG-TN-03-0010, Issue 1, Revision 5*, October 2004, 2004.
  - [27] P. Wessel and W. H. F. Smith, A global, self-consistent, hierarchical, high-resolution shoreline database, *J. Geophys. Res.*, vol. 101, pp. 8741–8743, 1996.